

# The dust condensation sequence in red super-giant stars

T. Verhoelst<sup>1,2,\*</sup>, N. Van der Zypen<sup>1</sup>, S. Hony<sup>3</sup>, L. Decin<sup>1,\*</sup>, J. Cami<sup>4</sup>, and K. Eriksson<sup>5</sup>

<sup>1</sup> Instituut voor Sterrenkunde, K.U. Leuven, Celestijnenlaan 200D, B-3001 Leuven, Belgium

<sup>2</sup> University of Manchester, Jodrell Bank Centre for Astrophysics, Manchester, M13 9PL, U.K.

<sup>3</sup> Laboratoire AIM, CEA/DSM - CNRS - Université Paris Diderot, DAPNIA/SAp, 91191 Gif sur Yvette, France

<sup>4</sup> Physics and Astronomy Dept, University of Western Ontario, London ON N6A 3K7, Canada

<sup>5</sup> Institute for Astronomy and Space Physics, Box 515, 75120 Uppsala, Sweden

Received / Accepted

## ABSTRACT

**Context.** Red super-giant (RSG) stars exhibit significant mass loss through a slow and dense wind. They are often considered to be the more massive counter-parts of Asymptotic Giant Branch (AGB) stars. While the AGB mass-loss is linked to their strong pulsations, the RSG are often only weakly variable. This raises the question whether their wind-driving mechanism and the dust composition in the wind are the same.

**Aims.** To study the conditions at the base of the wind, by determining the dust composition in a sample of RSG. The dust composition is thought to be sensitive to the density, temperature and acceleration at the base of the wind. To compare the derived composition with the composition found in AGB star winds.

**Methods.** We compile a sample of 27 RSG infrared spectra (ISO-SWS) and supplement these with photometric measurements to obtain the full spectral energy distribution (SED). These data are modelled using a dust radiative transfer code, taking into account the optical properties of relevant candidate materials. The results are scrutinised for correlations in terms of mass-loss rate, density at the inner edge of the dust shell and stellar parameters.

**Results.** We find (1) strong correlations between dust composition, mass-loss rate and stellar luminosity, roughly in agreement with the theoretical dust condensation sequence, (2) the need for a continuous (near-)IR dust opacity and tentatively propose amorphous carbon, and (3) significant differences with AGB star winds: presence of PAHs, absence of 'the' 13  $\mu$ m band, and a lack of strong water bands.

**Conclusions.** Dust condensation in RSG is found to experience a similar freeze-out process as in AGB stars. Together with the positive effect of the stellar luminosity on the mass-loss rate, this suggests that radiation pressure on dust grains is an important ingredient in the driving mechanism. Still, differences with AGB stars are manifold and thus the winds of RSG deserve separate studies.

**Key words.** stars: circumstellar matter, stars:supergiants, stars:winds, outflows, stars:atmospheres, infrared:stars

## 1. Introduction

As stars of initial mass  $8 \leq M_{\text{init}} \leq 40 M_{\odot}$  evolve off the main sequence and reach the core helium-burning phase, they turn into red super-giant (RSG) stars, the largest and most luminous of all stars (for a recent review on massive star observation and evolution, see Massey 2003). Through their stellar wind and eventually when they end their life through a supernova explosion, they enrich the ISM with heavy elements and large amounts of kinetic energy, possibly triggering new star formation (Gehrz 1989; Herbst & Assousa 1977). The dusty stellar winds of RSG not only influence their evolution, but also complicate the determination of general properties such as the effective temperature and surface gravity, e.g. through reddening which appears different from that through the ISM (Massey et al. 2005).

Most RSG are irregular variables with smaller amplitudes and higher effective temperatures than AGB stars. Moreover, they often show significant chromospheric activity. These properties make them intrinsically very different from their lower-mass counterparts in which strong pulsations and cool molecular layers are believed to be crucial ingredients for the mass loss

(Hoefner et al. 1998, and further updates). Instead, convection, rotation and/or chromospheric activity may turn out to play an important role. For example, Josselin & Plez (2007) find a correlation between mass-loss rate and the strength of the photospheric turbulence.

While the mechanism responsible for the initial levitation of the atmosphere may therefore be different in RSG as compared to AGB stars, both types of stars are often used together in studies of the dust condensation sequence and wind driving mechanism (e.g. Matsuura et al. 2005; Dijkstra et al. 2005). Nevertheless, Speck et al. (2000) find differences in dust composition between RSG and AGB stars, with the former often showing Ca-Al-rich silicates instead of magnesium silicates.

Assuming a dust condensation sequence such as that presented by Tielens (1990) and placing it in an expanding stellar wind, one expects a process called “freeze-out”, where the sequence is not completed but stops at an intermediate product when the wind density drops below the density required for the next step. This freeze-out is now tentatively observed in AGB stars (e.g. Heras & Hony 2005). If the dust condensation and the wind dynamics are similar for the RSG, one may also expect to observe incomplete dust condensation. We test this hypothesis through the analysis of all ISO-SWS spectra of RSG.

Send offprint requests to: T. Verhoelst, e-mail: [tijl.verhoelst@ster.kuleuven.be](mailto:tijl.verhoelst@ster.kuleuven.be)

\* Postdoctoral Fellow of the Fund for Scientific Research, Flanders

In Sect. 2, we present the construction of the sample and its main characteristics. Sect. 3 deals with the reduction of the ISO-SWS spectra. In the following section, we discuss the details of our modelling strategy, including the photosphere models, dust components, radiative transfer method and fitting strategy. In Sect. 5.1, we analyse an “averaged” RSG dust spectrum to check for any major short comings in our modelling approach. The results on all individual sample stars are then summarised in Sect. 5.2 and trends and correlations between the derived parameters are presented. The discrepancies between models and observed spectra are studied in Sect. 6. We end with a discussion and the conclusions (Sect. 8).

## 2. The sample

The availability of an ISO-SWS spectrum is an essential ingredient for our research aims and the first step is therefore the selection of all stars with spectral types M and K and luminosity classes I and II from the list of usable 2.4–45  $\mu\text{m}$  ISO-SWS spectra presented by Sloan et al. (2003). From this list of 41 stars, we remove the RV Tauri star R Sct as it is a Post-AGB object. The spectra of XX Per, IRC +60370 and WX Cas show technical anomalies and are also removed from our list. Distances are derived from the HIPPARCOS parallax measurement (Perryman et al. 1997) or from the assumed distances to the clusters containing our program stars (Humphreys 1978). For IRC+40427, no reliable distance estimate is available. We assume it to be a typical 2 kpc, which may in fact be too nearby, as the observed reddening is much stronger than the combined effect of that distance and its circumstellar shell (see Sect. 5.2). As the strong reddening may also be a consequence of a non-spherical distribution of the circumstellar dust, we refrain from deriving a distance from the observed reddening.

Effective temperatures and bolometric corrections are estimated from the spectral type based on the relations found by Levesque et al. (2005). Comparison with the evolutionary tracks of Lejeune & Schaerer (2001) reveals 24 bona fide red supergiants, and 3 strong candidates<sup>1</sup>. VY CMa is an RSG experiencing extreme mass loss resulting in an optically thick circumstellar environment (CSE). The detailed analysis required to derive reliable dust composition parameters for VY CMa is beyond the scope of this paper, and we refer to Harwit et al. (2001) for a study of its ISO-SWS spectrum.

We use these 26 stars for our study. Their designations and main characteristics are presented in Table 1. The overlap with the samples of Sylvester et al. (1994), Speck et al. (2000) and Levesque et al. (2005) is 8, 11 and 14 stars, respectively.

Kraemer et al. (2002) present a classification of, amongst others, our sample stars on the basis of their photospheric and dust characteristics. Most stars are in the 2.*SEa*, 2.*SEb* or 2.*SEc* classes, meaning they show strong dust features from silicates and alumina, and molecular bands in the photospheric part of the spectrum.

## 3. The observations

The Infrared Space Observatory Short Wavelength Spectrometer (ISO-SWS Kessler et al. 1996) observations were done in the AOT1 observing mode, resulting in a low-resolution full grating scan, except for S Per, which was observed at full instru-

mental resolution in the AOT06 mode. The observations were then processed using the SWS interactive analysis product, IA (see de Graauw et al. 1996) using calibration files and procedures equivalent to pipeline version 10.1. Further data processing consisted of extensive bad data removal and rebinning on a fixed resolution ( $\lambda/\Delta\lambda=200$ ) wavelength grid. The bad data-removal uses the large amount of redundancy in the available spectral scans to identify cosmic hits, sudden changes in dark-current and other artifacts that cause the signal of a single or multiple detectors to diverge from the mean of the other spectral scans. In order to combine the different subband into one continuous spectrum from 2 to 45  $\mu\text{m}$  we have applied scaling factors or offsets. In general the match between the different subbands is good and the applied scaling/offsets are small compared to the flux calibration uncertainties with a few exceptions: Alpha Her and NR Vul show much larger differences between the different subbands than can be expected on the basis of the flux-calibration uncertainties alone. This is most likely due to mispointed observations. For these two observations we use the IRAS point-source fluxes as a guideline for splicing the spectrum. The RMS noise increases with increasing wavelength, in particular at  $\lambda > 27 \mu\text{m}$ . The flux levels of our sample stars drop with wavelength, in particular if there is little or no dust excess. This causes some of the longest wavelength parts of the spectra to be noise dominated. See as the worst example H 14580 in Fig. 2. The noise-dominated parts are not used in the analysis.

For a proper estimation of the photospheric irradiation and underlying continuum, we prefer to construct a spectral energy distribution (SED) covering wavelengths from the UV to the far-IR. Optical photometry can be found in Johnson et al. (1966a), Johnson et al. (1966b), Mendoza (1967), Lee (1970), Cousins & Lagerweij (1971), Humphreys & Ney (1974), Wawrukiewicz & Lee (1974), Nicolet (1978) and Kharchenko (2001). Near-IR photometry is available for all our sources from the 2MASS catalogue (Skrutskie et al. 2006) and the far-IR side of the SED can be covered with the IRAS observations which are available for all but seven of our sources (Neugebauer et al. 1984).

Using interstellar extinction estimates from either the model by Arenou et al. (1992) or from the observed extinction towards the early-type stars in the corresponding clusters, we deredden the photometric and spectroscopic data with the law presented by Cardelli et al. (1989), extended toward longer wavelengths with the local ISM curve of Chiar & Tielens (2006), and assuming  $R_V = 3.6$  (Massey et al. 2005).

## 4. Modelling

The focus of this study is to derive accurate dust masses and its composition. Therefore, several aspects of the complex RSG atmospheres are not taken into account and the following simplifications are made constructing the radiative transfer models: (1) all calculations are done in 1D-spherical geometry, which means we neglect inhomogeneities, (2) we do not take the chromosphere into account, (3) we do not include any extra-photospheric molecular layers and (4) we assume the mass loss to be constant.

### 4.1. Photospheres

The stellar photospheres are represented by MARCS (edition 1998) models (Gustafsson et al. 2008) as these are specifically developed for cool stars, with an emphasis on molecular opacities and the effects of extended atmospheres which do not allow a

<sup>1</sup> Stars removed from the list because they are either on the AGB or even on the RGB: T Cet, WX Cas, BD+59 594,  $\iota$  Aur, HD 90586, RT Car, BC Cyg, CIT 11 and IRC+60370,  $\beta$  Cap, S Pav and  $\alpha$  UMa

**Table 1.** Object designations and general characteristics. Star with their names printed in *italic* have luminosities which also allow an AGB star identification. The bolometric magnitudes were computed from the dereddened K band magnitudes, using the bolometric corrections of Levesque et al. (2005).

Source	ISO TDT number	Spectral Type	Variability <sup>a</sup> Type	Period <sup>a</sup> [d]	Kraemer <sup>b</sup> class	Distance <sup>c</sup> [pc]	A <sub>V</sub> <sup>d</sup>	M <sub>bol</sub>
HD 14242	61301202	M2Iab	Lc		2.SEa:	2290	1.63	-6.93
AD PER	78800921	M2.5Iab	SRc	363	2.SEa:	2290	1.63	-7.42
HD 14404	45501704	M1Iab	Lc		2.SEap:	2290	1.63	-7.23
SU PER	43306303	M3Iab	SRc	533	2.SEc	2290	1.63	-7.90
RS PER	45501805	M4Iab	SRc	245	2.SEc	2290	1.63	-7.74
S PER	42500605	M4.5Iab	SRc	822	3.SE	2290	1.63	-8.18
HD 14580	42701401	M1Iab	Lc		1.NO:	2290	1.63	-6.49
HD 14826	61601203	M2Iab	Lc		2.SEa:	2290	1.63	-7.36
YZ PER	47301604	M2Iab	SRb	378	2.SEc	2290	1.63	-7.50
W PER	63702662	M4.5Iab	SRc	485	2.SEc	2290	1.63	-7.74
<i>RHO PER</i>	79501105	M4II	SRb	50	1.NO	100	0.82	-4.20
<i>HR 1939</i>	86603434	M2Iab	Lc		2.SEa	420	0.66	-4.51
ALF ORI	69201980	M2Iab	SRc	2335	2.SEc	131	0.09	-7.19
<i>HD 90586</i>	25400410	M2Iab/Ib			2.SEc	641	0.40	-4.76
R CEN	07903010	M5IIevar	M	546	2.SEap	641	0.95	-6.94
ALF SCO	08200369	M1.5Iabb	Lc		2.SEc	185	0.72	-7.86
ALF HER	28101115	M5Iab	SRc		1.NOp	117	0.42	-5.99
<i>SIG OPH</i>	10200835	K3Iab			1.NO	360	0.68	-4.33
HR 7475	31601515	K4Ib	N:		1.NO	704	0.91	-5.87
NR VUL	53701751	K3Iab	Lc		2.SEc	2000	2.98	-8.01
BD+35 4077	73000622	M2.5Iab	Lc		2.SEb	1820	2.61	-7.48
RW CYG	12701432	M3Iab	SRc	550	2.SEc	1200	3.54	-7.77
IRC +40427	53000406	M1:Iab			2.SEap:	2000	1.79	-6.89
MU CEP	08001274	M2Ia	SRc	730	2.SEc	830	1.84	-8.86
V354 CEP	41300101	M2.5Iab	Lc		2.SEc	3500	2.00	-8.51
U LAC	41400406	M4Iab:e	SRc		2.SEc	3470	1.74	-8.30
PZ CAS	09502846	M3Iab	SRc	925	2.SEc	2510	2.11	-8.89

<sup>a</sup> Combined General Catalogue of Variable Stars (Kholopov et al. 1998).

<sup>b</sup> Kraemer et al. (2002)

<sup>c</sup> Distances below 1 kpc come from parallax measurements with HIPPARCOS (Perryman et al. 1997). Distances equal to 2 kpc are actually unknown and distances greater than 1 kpc are cluster distances from Humphreys (1978).  $\mu$  Cep is an exception: we use the distance of Humphreys (1978) instead of the poor parallax measurement.

<sup>d</sup> ISM extinction estimates for stars within 1 kpc come from the galactic model of Arenou et al. (1992). All other stars and  $\mu$  Cep have estimates based on the extinction toward early-type stars in the corresponding clusters.

plane-parallel approximation. They were computed in spherical geometry with solar abundances, a surface gravity<sup>2</sup> of  $\log g = 0.5$ , a microturbulent velocity  $v_{\text{turb}} = 2 \text{ km s}^{-1}$  and temperatures ranging from 3000 to 4500 K. The effective temperatures were derived from the spectral type following the relations from Levesque et al. (2005).

#### 4.2. Dust radiative transfer

The dust shell is modelled using the proprietary spherical radiative transfer code `MODUST` (Bouwman et al. 2000; Bouwman 2001). Under the constraint of radiative equilibrium, this code solves the monochromatic radiative transfer equation from UV/optical to millimetre wavelengths using a Feautrier type solution method (Feautrier 1964; Mihalas 1978). The code allows to have several different dust components of various grain sizes and shapes, each with its own temperature distribution.

<sup>2</sup> Lower gravity models failed to converge at the lowest temperatures which led us to adopt this value uniformly. The stellar mass of the models in this grid is only  $1 M_{\odot}$ , but at the resolution of our set of observations, the difference with higher-mass models would not be noticeable.

#### 4.3. Dust composition

We searched the literature for relevant dust species to include in our study. Speck et al. (2000) find in the RSG in their sample melilite, alumina and olivines<sup>3</sup>, but they do not need a  $13 \mu\text{m}$ -carrier candidate such as Spinel as they do not detect this feature in their RSG spectra and neither do we (see Sect. 6). Heras & Hony (2005) find in their sample of AGB stars those species used by Speck et al. (2000) and also  $\text{Mg}_{0.1}\text{Fe}_{0.9}\text{O}$ , which has a feature at  $19.5 \mu\text{m}$ , outside the wavelength band observed by Speck et al. (2000). Cami (2002) uses olivines, alumina, spinel and  $\text{Mg}_{0.1}\text{Fe}_{0.9}\text{O}$ . For a discussion as to the need for melilite instead of an iron-magnesium silicate in RSG, we refer to Speck et al. (2000), who show the existence of a category of RSG 10 micron spectra with a peak position significantly to the red of that of olivines. Moreover, they show an excellent agreement with a predicted melilite emission spectrum.

From a theoretical point of view, a dust formation scenario usually starts with  $\text{TiO}_2$  seeds, on which first simple oxides such

<sup>3</sup> Remark that the term Olivine in principle refers to the crystalline form. Although the correct phrasing should be “amorphous silicate with an olivine stoichiometry”, we refer to this material as Olivines, as is done in similar studies.

as  $\text{Al}_2\text{O}_3$  and  $\text{MgFeO}$  grow. If the density/temperature conditions are right, also melilite, and olivines and pyroxenes with iron content can condense onto the grains. The full condensation scheme consists of quite a few more possible dust species (e.g. Anorthite and Plagioclase), but no spectral sign of these dust types has so far been seen in RSG.

The dust species used in this study and their relevant characteristics are presented in Table 2. The optical constants are obtained from the AIU Jena database<sup>4</sup>.

The RSG in this sample appear to be pure outflow sources, i.e. nothing indicates that they may be binary systems with stable circumbinary dust disks: as shown in Fig. 2, there is no strong discrepancy between reddening and IR excess, nor do we see any sign of processed, crystalline grains such as those seen around some Post-AGB objects (e.g. Gielen et al. 2007) or in protoplanetary disks (e.g. van Boekel et al. 2005). This implies that grain growth beyond  $0.1\,\mu\text{m}$  is unlikely (see e.g. Gail & Sedlmayr 1999; Woitke & Niccolini 2005). The absorption cross sections can therefore be calculated in the Rayleigh limit, and an underlying grain size distribution is only required to derive the dust masses. We use the size distribution derived by Mathis et al. (1977) and compute the cross section in the approximation of a Continuous Distribution of Ellipsoids (CDE, Bohren & Huffman 1983), as we found this to provide a better agreement with the observations than the Mie approximation. More sophisticated treatments of grain sizes and shapes exist now, such as a Distribution of Hollow Spheres (DHS), but within the Rayleigh limit, CDE works very well (Min et al. 2005). We must point out that according to very recent work by Höfner (2008), relaxing the restriction to the small particle limit in the modelling of AGB winds leads to a possible grain growth up to  $1\,\mu\text{m}$ , which may also help in the radiative driving of the wind.

An overview of the spectral features of these different dust species is shown in Fig. 1. An in-depth discussion of this figure is presented in Sect. 5.1.

#### 4.4. The strategy

The unknown angular scale of the central star is determined by scaling the model to the ISO-SWS spectrum between  $3.5$  and  $4.5\,\mu\text{m}$  as these wavelengths are relatively free of dust and molecular emission/absorption. This method allows us to bypass the uncertain absolute luminosity and distance. The geometrical properties of the dust shell are proportional to the stellar radius and thus their angular scale is now also fixed. Under the assumption of a continuous wind, the outer radius of the dust shell can not be determined from the current modelling as the outer regions of the wind are too cold to contribute to the Mid-IR spectrum. We therefore fix its value at  $5000\,R_\star$ .

The mass-loss rate does depend on the assumed distance and luminosity. The initial model grid (central star + dust shell) is calculated for a typical luminosity of  $10^5\,L_\odot$ . This model mass-loss rate  $\dot{M}_{\text{grid}}$  is converted to an actual  $\dot{M}$  using the distances presented in Sect. 2 and the angular scale derived from the fitting (see also Sect. 5.2). The outflow velocity and dust-to-gas ratio are assumed to be  $10\,\text{km s}^{-1}$  and  $0.01$  respectively, both typical values for RSG. Note that these are uncertain to a factor of at least 2.

The parameters to be determined from the individual fitting of the spectra are the inner radius,  $R_{\text{in}}$ , the mass-loss rate,  $\dot{M}$ , and the relative abundances of the different dust species.

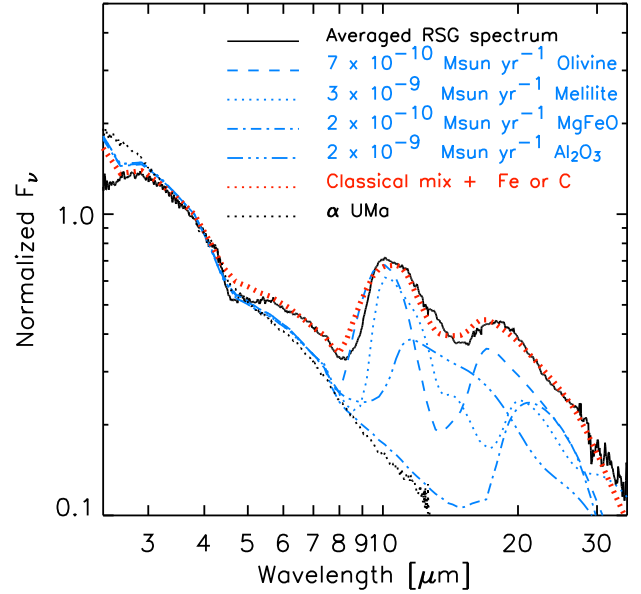


**Fig. 1.** The average of all dereddened observed dust spectra, each normalized with its photospheric flux at  $3.5\,\mu\text{m}$ . For comparison, the pure photospheric spectrum of  $\alpha$  UMa is shown as a black dotted line. The spectral features of the commonly used dust species are also shown (blue) in the way they appear in models with CSEs containing only that dust type. None of these dust species can explain the excess already observed before  $8\,\mu\text{m}$ . The red line is a model containing also some Fe and/or C.

We refrain from doing a formal minimisation while determining the optimum dust-shell parameters. Instead we determine the best-fit model using visual inspection, following a well defined strategy. The reasons for doing so are two-fold. 1) It is our aim to get, at the same time, a good fit to the SED **and** the detailed IR-spectrum. This is a requirement as the circumstellar reddening puts a strong constraint on the inner shell radius, which in turn determines the relative contribution of the individual dust species to the observed features through their different temperatures. It is virtually impossible to devise a good weighting scheme to give equal importance to the  $\sim 10$  photometric points and the thousands of spectral points in the SWS spectra. In particular, since the uncertainties on the data vary considerably throughout the sample, this would imply adapting the weighting on a per source basis. The only way to judge whether such a complicated weighting scheme works well would be by visual inspection. 2) There are some spectral regions that may be poorly reproduced even with a, to our judgement, good model. This is due to the possible presence of components in the real spectra which are lacking in the model, like extended molecular layers (also known as MOLspheres) or PAHs. Again, such regions and their importance can only be identified by visual inspection.

The core of our strategy is an iteration of the following sequence:

- We estimate the dust mass-loss rate from the full SED and the observed  $L_{\text{IR}}/L_\star$ <sup>5</sup>.

<sup>5</sup>  $L_{\text{IR}}$  is calculated as the integration over  $\lambda \geq 2\,\mu\text{m}$  of the final model spectrum minus the photospheric model and  $L_\star$  is calculated by integrating the photospheric model over all wavelengths.

<sup>4</sup> <http://www.astro.uni-jena.de/Laboratory/Database/databases.html>

**Table 2.** Dust species used in this study with their commonly-used name, their size, shape and the source of the optical constants. The size distribution is that derived by Mathis et al. (1977) and the cross section are computed in the CDE (Continuous Distribution of Ellipsoids) approximation.

Name	Composition	Lattice structure	Size ( $N(\alpha) \sim \alpha^{-3.5}$ )	Shape	Reference
Alumina	$\text{Al}_2\text{O}_3$	amorphous	0.01 – $1\mu\text{m}$	CDE	Begemann et al. (1997); Koike et al. (1995)
Melilite	$\text{Ca}_2\text{Al}_2\text{SiO}_7$	amorphous	0.01 – $1\mu\text{m}$	CDE	Mutschke et al. (1998); Jaeger et al. (1994)
Olivine	$\text{Mg}_{0.8}\text{Fe}_{1.2}\text{SiO}_4$	amorphous	0.01 – $1\mu\text{m}$	CDE	Dorschner et al. (1995)
MgFeO	$\text{Mg}_{0.1}\text{Fe}_{0.9}\text{O}$	amorphous	0.01 – $1\mu\text{m}$	CDE	Henning et al. (1995)
Metallic iron	Fe	crystalline	0.01 – $1\mu\text{m}$	CDE	Henning & Stognienko (1996)
Carbon	C	amorphous	0.01 – $1\mu\text{m}$	CDE	Preibisch et al. (1993)

- The relative abundances of melilite, olivine and alumina are adjusted to match the peak position of the  $10\mu\text{m}$  feature
- and the same is done for the  $18\mu\text{m}$  feature peak position using olivine, melilite and  $\text{Mg}_{0.1}\text{Fe}_{0.9}\text{O}$ .
- When the peak positions of the features are well reproduced but not yet their strength, we vary the inner radius to adjust their relative strenghts and the mass-loss rate to alter the absolute emission levels. Meanwhile, we check that our model predicts the correct amount of circumstellar reddening.

## 5. Results

### 5.1. A continuum opacity source

In Fig. 1, we present an “averaged” RSG ISO-SWS spectrum, where each individual spectrum is dereddened with the appropriate value (last column in Table 1) and normalized to the average flux between 3.5 and  $4\mu\text{m}$ . We exclude RSG without significant mass loss. Also shown are models with envelopes containing only a single dust type.

Striking in this figure is that the observed excess appears to start already at  $5\mu\text{m}$ , while the modelled dust features are all located beyond  $8\mu\text{m}$ . A related problem could be the slope of the photospheric(?) part of the modelled spectrum at  $2.5\text{--}3\mu\text{m}$ .

The excess around  $6\mu\text{m}$  and the difference in slope around  $3\mu\text{m}$  have recently been attributed to the presence of a MOLsphere, i.e. an extra-photospheric layer of molecular material (e.g. Tsuji 2000), in which especially  $\text{H}_2\text{O}$  would be the main source of excess emission and absorption. Individual lines of water in these MOLspheres have been detected (e.g. Jennings & Sada 1998) and the shells have been resolved by near and mid-IR interferometry (e.g. Perrin et al. 2004; Ohnaka 2004; Perrin et al. 2005). Verhoelst et al. (2006) argue that a purely molecular MOLsphere cannot explain the wavelength dependence of the opacity across the entire IR range in the case of RSG  $\alpha$  Ori and they suggest alumina as additional mid-IR opacity source. However, this does not yet explain the observation made by Ryde et al. (2006) in the spectra of  $\mu$  Cep, that water lines appear in absorption at  $12\mu\text{m}$ , while they are assumed to generate an excess at  $6\mu\text{m}$ <sup>6</sup>. Moreover, the excess around  $6\mu\text{m}$  in the individual stars does not show any water lines in proportion to the excess w.r.t. the photospheric continuum.

We propose here that, although extra-photospheric molecular material is clearly present, the peculiarities in the shape of the overall SED discussed here are due to a source of continuous opacity with a fairly cool temperature. Free-free emission from a chromosphere or ionised wind can be present in RSG

(e.g. Harper et al. 2001), but since its source function has a temperature above that of the photosphere, it can not explain the additional extinction towards the near-IR<sup>7</sup>. The color temperature of the excess therefor points to dust rather than free-free emission. We find that the inclusion of either metallic Fe, amorphous C or micron-sized grains in the dust shell can explain the excess emission at  $6\mu\text{m}$ , the slope issue at  $3\mu\text{m}$  and the additional extinction at near-IR wavelengths (see Sect. 5.2). The remaining residuals are molecular absorption, as expected from the presence of a cool MOLsphere.

Whether this missing dust species is either metallic iron, micron-sized grains or amorphous carbon, can not be fully answered with the current analysis. The presence of metallic Fe in the CSE of VY CMa has been postulated by Harwit et al. (2001) and it is also used to explain the SEDs of OH/IR stars (Kemper et al. 2002). Moreover, metallic Fe is a product of the O-rich condensation sequence. Nevertheless, amorphous carbon is an equally interesting possibility, as it would be roughly 20 times as effective in accelerating the wind as Fe (see Table 1 in Woitke 2006). The occurrence of pure carbon in an oxygen-rich CSE is plausible (Höfner & Andersen 2007), even more so in RSG where the chromospheric radiation field can be responsible for the dissociation of CO. We find that, for the amount of pure carbon required to explain the RSG spectra, only of the order of 1 % of the CO must be dissociated. This is well below what is found possible in theoretical models of M stars with chromospheres (Beck et al. 1992). More evidence for the presence of carbon not bound in CO is the detection of PAH emission in four of our sources (Sect. 6.2.3). Papers discussing the possible presence of amorphous carbon in oxygen-rich outflows often dismiss the spectroscopic detection of its presence as impossible due to the lack of spectral features. Interestingly, we find here that, when studying the full SED, it is possible to detect continuous opacity sources. Continuous opacity by micron-sized O-rich grains, playing a crucial role in the driving of the wind, has been proposed for AGB stars by Höfner (2008), but it is unclear whether this grain growth can also occur in RSG.

Regardless of the origin of this continuum emission, it must be included in our modelling to derive reliable mass fractions for the other dust species. We have chosen to include amorphous C, in the knowledge that Fe would have a similar effect.

### 5.2. Models for all sample stars

Figures 2 and 3 present the observed SEDs and spectra respectively and the best-fit models, sorted following increasing dust

<sup>6</sup> The MOLspheres are found to be colder than the photospheric background, and generate excess emission only through their larger emitting surface.

<sup>7</sup> We know that the near-IR is suffering additional extinction (as opposed to less excess emission) from the fit of our photosphere models to the unreddened optical fluxes

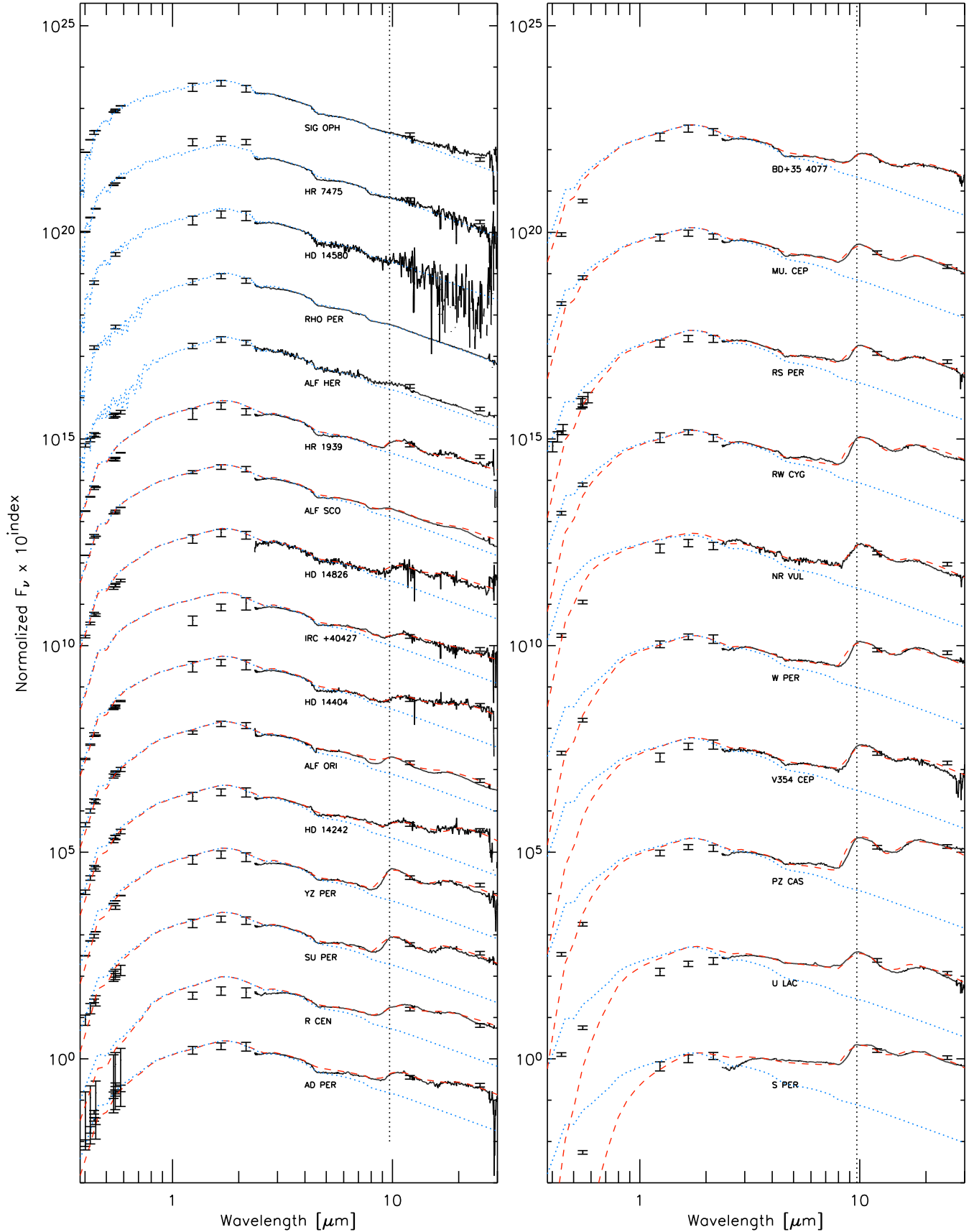


**Fig. 2.** The SEDs of all sample stars with their best-fit models (total spectrum in red dashes and non-reddened photospheric spectrum in blue dots). The photometric points are either the 7 Geneva filters or B and V in the Johnson system, J H and Ks from 2mass and I12 and I25 from the IRAS mission. The dotted vertical line indicates  $9.7 \mu\text{m}$ , the wavelength where “classical” amorphous silicates

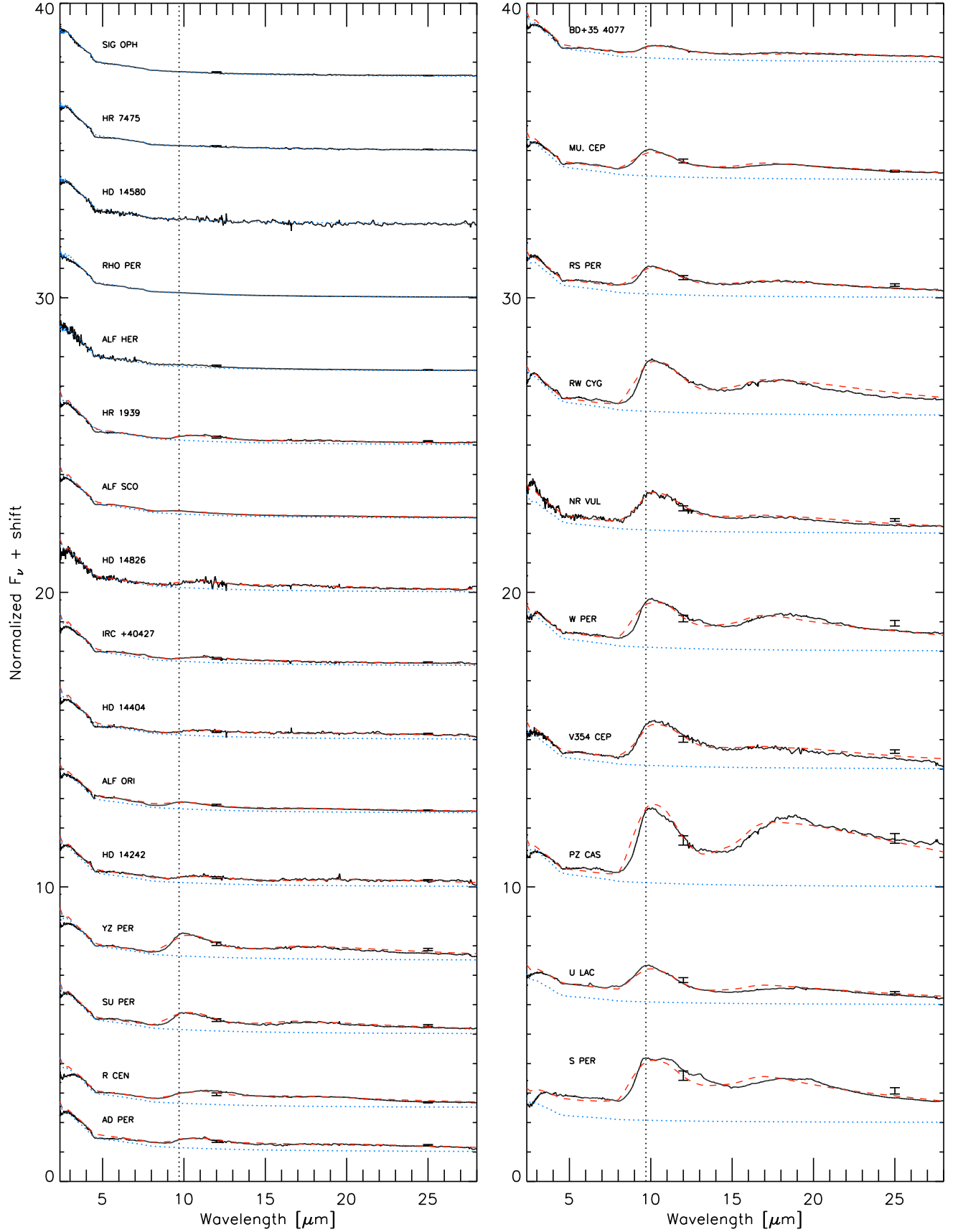


**Fig. 3.** The ISO-SWS spectra of all sample stars with their best-fit models (symbols and colours as in Fig. 2).



luminosity or following decreasing photospheric temperature in case no dust emission is present. In general the agreement is excellent. IRC +40427 appears much more reddened than our estimate of  $A_V = 1.79$ , which suggests it to be located much further away than our default value of 2 kpc.

The results on all 27 sample stars are summarized in Table 3. For 6 objects, the mass-loss rate is too low ( $\dot{M} \leq 10^{-9} M_\odot \text{yr}^{-1}$ ) to allow for a reliable determination of the dust composition. The distance and luminosity corrected mass-loss rate presented in column 9 is computed as

$$\dot{M} = \dot{M}_{\text{grid}} A (d/1 \text{ kpc})^2$$

where  $\dot{M}_{\text{grid}}$  is the mass-loss rate for an assumed luminosity of  $10^5 L_\odot$  (the default value in our model grid),  $A$  is the scaling factor used to match the observed flux around  $4 \mu\text{m}$  and  $d$  is the distance.

## 6. Analysis of the residuals

A general problem, especially for the higher mass-loss stars, is the over-prediction of the near-IR photometry. This corresponds to the need for an extinction law with a higher  $R_V$ . The dust already includes a component with grey extinction properties (see Sect. 5.1), but in our models it is located too far from the central star to provide sufficient extinction. Our model assumes the same inner radius for all dust species, but the discrepancy observed here may indicate that the continuous opacity source is located even closer to the base of the wind, right above the photosphere. The detection of alumina  $0.5 R_\star$  above the photosphere of Betelgeuse (Verhoelst et al. 2006; Perrin et al. 2007) shows that dust condensation so close to the photosphere is possible.

### 6.1. Molecular bands

The ISO spectra up to  $8 \mu\text{m}$  are dominated by photospheric and possibly continuum dust emission. The observed spectral features should therefore mainly be photospheric molecular absorption bands. To search for evidence for the presence of the MOLsphere(s) discussed in Sect. 5.1 or for indications of shortcomings in our model atmospheres, we compare the average normalized<sup>8</sup> residuals with simulated molecular absorption bands in Fig. 4. Although our models clearly match the observed spectra very well (the better part of the residuals does not reach a 5% level), we detect strong additional absorption by CO and maybe also some water and OH. The latter two discrepancies can probably be solved by more detailed fine tuning of the atmosphere models. Cool CO appears to be very abundant also above the photosphere, which is in line with a postulated crucial role in the wind-driving mechanism. The fact that no massive MOLspheres containing water are observed clearly sets the RSG apart from the AGB stars. This finding supports our assumption (Sect. 5.1) that the excess at  $6 \mu\text{m}$  and the slope issue at  $3.5 \mu\text{m}$  is due to some continuum emission source and not an extra-photospheric water column.

### 6.2. Residual dust features

The lower panel of Fig. 4 shows the average residuals in the dust-dominated part of the spectrum. Many discrepancies are clear:

<sup>8</sup> Normalization of each observed and model spectrum was done by inverse scaling with the average flux ( $F_\nu$ ) between  $3.5$  and  $4 \mu\text{m}$ . The spectra were then subtracted, and the residuals calculated in this way averaged over the sample.

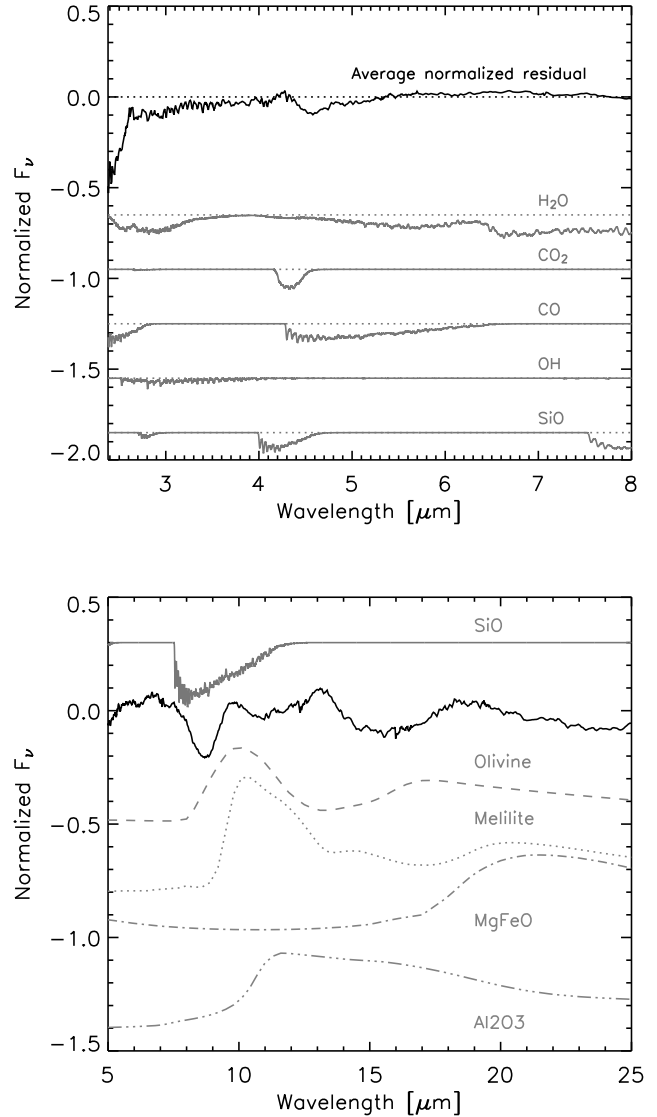


**Fig. 4.** *Upper panel:* The average normalized residuals in the blue part of the ISO-SWS spectrum together with simulated molecular absorption bands. For more details on the computation of the molecular templates we refer to Cami (2002). *Lower panel:* The wavelength range of the residuals (black solid line) which is dust dominated.

(1) a strong absorption band starting at  $8 \mu\text{m}$  and possibly extending up to  $12 \mu\text{m}$  if we interpret the emission bump at  $9.7 \mu\text{m}$  as an underestimated olivine dust fraction, (2) a broad  $13 \mu\text{m}$  feature and (3) a broad emission feature at  $18 \mu\text{m}$ . Concerning the first problem: a significant SiO layer just above the photosphere, which deepens the absorption band, could be present as such a layer is detected around  $\alpha$  Ori with MIDI interferometry by Perrin et al. (2007), but the SiO bandhead does not correspond very well with the observed residuals around  $8 \mu\text{m}$ . It may also be that the current dust model does not yet contain the right silicate dust composition/shape/grain size.



**Table 3.** The best fit model parameters.

Source	Spectral Type	$T_{\text{eff}}$ [K]	Melilite % -mass	Olivine % -mass	Alumina % -mass	Mg <sub>0.1</sub> Fe <sub>0.9</sub> O % -mass	Carbon % -mass	$R_{\text{in}}$ [ $R_{\star}$ ]	$M_{\text{model}}$ [ $M_{\odot} \text{ yr}^{-1}$ ]	$M$ [ $M_{\odot} \text{ yr}^{-1}$ ]	$L_{\text{IR}}/L_{\star}$
NR VUL	K3Iab	4015	0.56	0.19	0.24	0.00	0.013	10	3.1e-07	2.7e-07	0.074
SIG OPH	K3Iab	4015									
HR 7475	K4Ib	3900									
IRC +40427	M1:Iab	3745	0.43	0.00	0.55	0.00	0.018	15	1.1e-07	5.0e-08	0.011
HD 14580	M1Iab	3745									
HD 14404	M1Iab	3745	0.48	0.00	0.48	0.04	0.007	15	1.5e-07	7.7e-08	0.012
ALF SCO	M1.5Iab	3710	0.74	0.09	0.12	0.00	0.049	13	4.1e-08	3.3e-08	0.009
MU. CEP	M2Ia	3660	0.31	0.27	0.41	0.00	0.020	18	2.9e-07	7.9e-07	0.048
HD 90586	M2Iab/Ib	3660	0.57	0.14	0.23	0.05	0.011	10	1.4e-07	8.5e-09	0.020
ALF ORI	M2Iab	3660	0.64	0.16	0.20	0.00	0.001	13	6.3e-08	2.9e-08	0.022
HR 1939	M2Iab	3660	0.82	0.01	0.16	0.00	0.003	10	1.1e-07	6.1e-09	0.006
YZ PER	M2Iab	3660	0.60	0.14	0.26	0.00	0.003	18	3.5e-07	2.7e-07	0.026
HD 14826	M2Iab	3660	0.42	0.05	0.52	0.00	0.005	15	1.7e-07	1.0e-07	0.010
HD 14242	M2Iab	3660	0.59	0.00	0.34	0.05	0.017	15	1.8e-07	7.2e-08	0.023
V354 CEP	M2.5Iab	3615	0.57	0.14	0.28	0.00	0.008	11	5.6e-07	9.8e-07	0.087
BD+35 4077	M2.5Iab	3615	0.78	0.03	0.16	0.02	0.010	15	2.9e-07	2.0e-07	0.029
AD PER	M2.5Iab	3615	0.59	0.03	0.34	0.02	0.017	15	2.4e-07	1.5e-07	0.029
RW CYG	M3Iab	3605	0.53	0.17	0.30	0.00	0.002	25	1.0e-06	9.4e-07	0.069
PZ CAS	M3Iab	3605	0.40	0.30	0.30	0.01	0.002	40	1.7e-06	5.4e-06	0.109
SU PER	M3Iab	3605	0.39	0.19	0.39	0.03	0.008	15	2.6e-07	3.0e-07	0.027
U LAC	M4Iab:e	3535	0.25	0.44	0.25	0.01	0.053	10	3.7e-07	9.0e-07	0.154
RHO PER	M4II	3535									
W PER	M4.5Iab	3535	0.09	0.27	0.63	0.00	0.009	20	7.8e-07	6.4e-07	0.085
S PER	M4.5Iab	3535	0.03	0.27	0.68	0.01	0.022	15	1.8e-06	2.2e-06	0.302
RS PER	M4Iab	3535	0.42	0.21	0.31	0.04	0.017	13	3.8e-07	4.2e-07	0.063
ALF HER	M5Iab	3450									
R CEN	M5Iivar	3450	0.33	0.06	0.60	0.00	0.009	15	3.7e-07	3.3e-07	0.028

### 6.2.1. A 13 $\mu\text{m}$ feature?

Speck et al. (2000) find in their analysis that RSG usually do not display the 13  $\mu\text{m}$  feature as seen in AGB stars. We find in general, after model subtraction, a feature around 13  $\mu\text{m}$ , but it is much broader than the one seen in the lower-mass counterparts. Only a few selected targets display the AGB-like 13  $\mu\text{m}$  feature, but these stars (SU Per and S Per) may be different in other aspects as well: S Per is the only target in our sample showing strong water bands, and Speck et al. (2000) already suggested it to be more similar to lower-mass semi-regulars. The broad excess in the residual spectrum can not be isolated in any of the spectra prior to model subtraction. Therefore, it can not be positively identified as a component, but might be due to some systematic problem with our models. The most likely systematic effect to cause such an underprediction would be a lack of absorptivity in one of the sets of optical properties that we have used.

### 6.2.2. The 18 $\mu\text{m}$ feature

The 18  $\mu\text{m}$  feature observed in the residuals is most probably the feature typical ascribed to the silicates generating the 9.7  $\mu\text{m}$  feature (the olivines). However, starting from laboratory-measured optical constants, we find it impossible to reproduce this peak position: either it is blue shifted (olivines) or it peaks to the red (melilite). The inclusion of either alumina or MgFeO causes the model emission band to be centered at the observed wavelength. However, this always causes a double peaked band profile which is never observed. We note that this discrepancy is not unique to the RSG but is also found in the AGB stars with optically thin

dust shells as studied by Heras & Hony (2005). This problem may be related to that at 8  $\mu\text{m}$ .

### 6.2.3. Detection of PAHs

As shown in Fig. 5, we clearly detect PAH emission bands at 6.3, 7.6, 11.3 and 14.2  $\mu\text{m}$  in 3 stars: AD Per, IRC 40427, and U Lac. RS Per only shows a significant PAH feature at 7.6  $\mu\text{m}$ . AD Per and IRC 40427 also show a feature at 12.7  $\mu\text{m}$ . The PAHs in AD Per, RS Per and IRC 40427 were already detected by Sylvester et al. (1994, 1998) who relate their presence with the dissociation of CO molecules by the UV radiation field of the chromosphere, as no PAHs are detected in AGB stars. The diffuse ISM is known to show PAH emission features but we are confident that the bands observed here originate in the CSE of the RSG since 1) the observed bands are as strong in the UKIRT observations of Sylvester et al. (1994) as in our ISO-SWS observations, in spite of a different aperture, 2) the UKIRT observations used a chopping technique, which should remove a large fraction of an extended ISM feature and 3) the relative band strengths do not agree with those of the ISM and the 6.22  $\mu\text{m}$  feature is, in some cases, shifted to longer wavelengths.

Using the dust shell models presented here, we are able to isolate the PAH emission features. This allows us to study the band shapes and strengths in a manner similar to Peeters (2002) and Hony et al. (2001). Such an analysis can yield important information on the structural properties of the PAH family and give clues about their formation conditions. This analysis is left to a future study. Perusal of Fig. 5 already shows that the PAH features in our sample span an interesting range both in which bands are observed, band strength ratios and band-shapes.

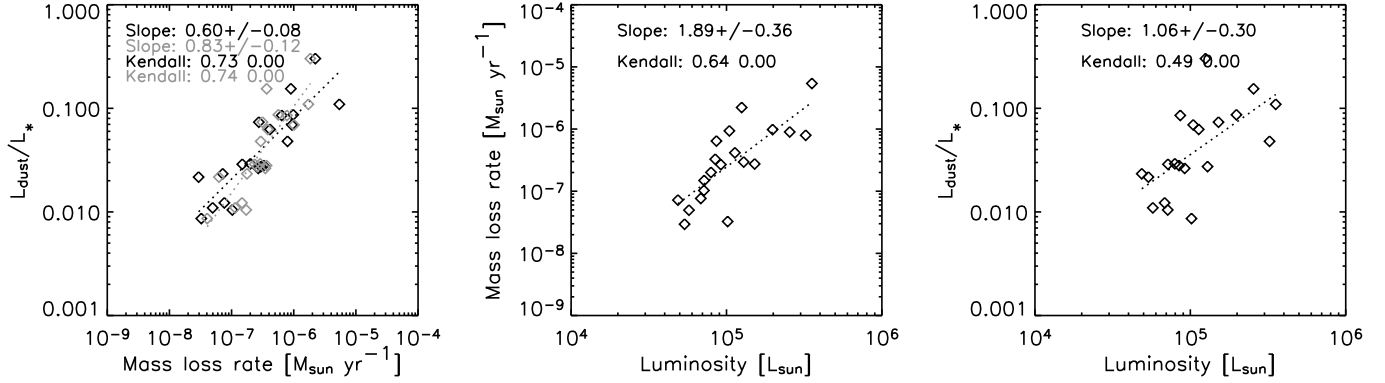


**Fig. 6.** *Left panel:* The correlation between mass-loss rate and the ratio of dust to photospheric luminosity. The slope is that of a linear fit, the Kendall values refer to the Kendall rank correlation value and its significance. The Kendall rank correlation  $\tau \equiv \frac{n_c - n_d}{\frac{1}{2}n(n-1)}$  where  $n$  is the size of the sample,  $n_c$  is the number of concordant pairs and  $n_d$  is the number of discordant pairs. The significance is a value in the interval  $[0.0, 1.0]$  where a small value indicates a significant correlation. The relation is clear using both  $\dot{M}_{\text{grid}}$  (grey symbols) and the distance-corrected mass-loss rate (black symbols). *Middle panel:* Mass-loss rate (corrected for luminosity and distance) versus stellar luminosity. *Right panel:* The luminosity- and distance-independent mass-loss indicator versus stellar luminosity. Only stars which are certainly RSG were used to measure these correlations.

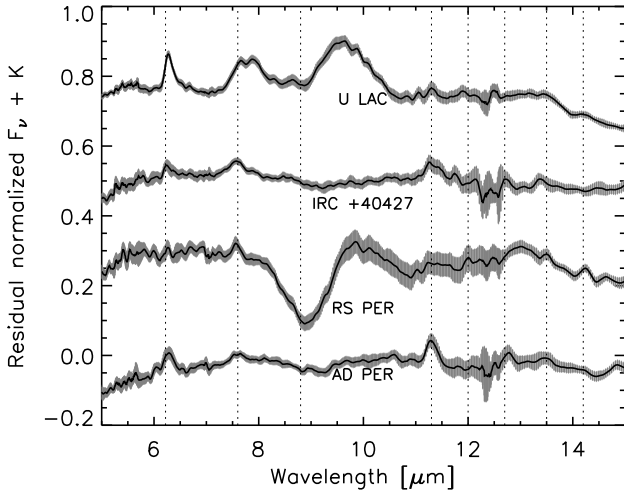


**Fig. 5.** The 5 to 15  $\mu\text{m}$  spectra of RSG showing PAH emission. The grey error bars correspond to  $3\sigma$ . Known PAH feature wavelengths are indicated with a dashed line. These wavelengths are taken from Hony et al. (2001) and Peeters (2002).

## 7. Analysis

### 7.1. $L_{\text{dust}}/L_{\star}$ as mass-loss rate indicator

Column 10 presents the ratio between dust and photospheric luminosity. This ratio can be used as a distance-independent mass-loss indicator, which is not trivial, as it must be checked that the variation of  $L_{\text{dust}}/L_{\star}$  over the sample is due to different mass-loss rates and not only a difference in dust composition, e.g. the oxides tend to generate much less emission than the magnesium-rich silicates, for a similar dust mass. We show our derived relation between  $L_{\text{dust}}/L_{\star}$  and mass-loss rate, based on our modelling including the differences in dust composition, in the left hand panel of Fig. 6. When assuming an identical luminosity for

all stars, we find an almost one-to-one relation between mass-loss rate and dust luminosity fraction. This shows that  $L_{\text{dust}}/L_{\star}$  is a good mass-loss indicator. When correcting for distance and stellar luminosity, the relation is less steep. This is a consequence of the correlation between stellar luminosity and mass-loss rate discussed in the next section.

### 7.2. A correlation between mass-loss rate and stellar luminosity

The middle panel of Fig. 6 shows a strong correlation between mass-loss rate and stellar luminosity and therefore also with stellar mass. The best-fit linear relation is:

$$\dot{M} = 10^{-16.2 \pm 1.8} L_{\star}^{1.89 \pm 0.36}.$$

As an increase of the mass-loss rate with luminosity, i.e. size of the object, is expected just from scaling arguments, we also show the dust luminosity fraction as a function of stellar luminosity (right hand panel of Fig. 6). Interestingly, we find evidence for a more efficient wind-driving mechanism in the more luminous stars. The best-fit linear relation here is:

$$L_{\text{IR}}/L_{\star} = 10^{-7.5 \pm 1.7} L_{\star}^{1.06 \pm 0.30}.$$

We note also that we do not find a significant trend between mass-loss rate and effective temperature.

### 7.3. Dust composition as a function of mass-loss rate

A purely empirical indication of the relation between mass-loss rate and dust composition can be obtained by simply plotting peak position of the 10- $\mu\text{m}$  complex versus dust luminosity. This is done in the upper left panel of Fig. 7. With increasing mass-loss rate, the peak position shifts from 11 to 10  $\mu\text{m}$ . For intermediate values (e.g. BD+35 4077, see top right in Fig. 2), it is difficult to assign a single peak wavelength.

We search for correlations between dust composition and mass-loss rate based on our modelling and find the following trends with increasing mass-loss rate:

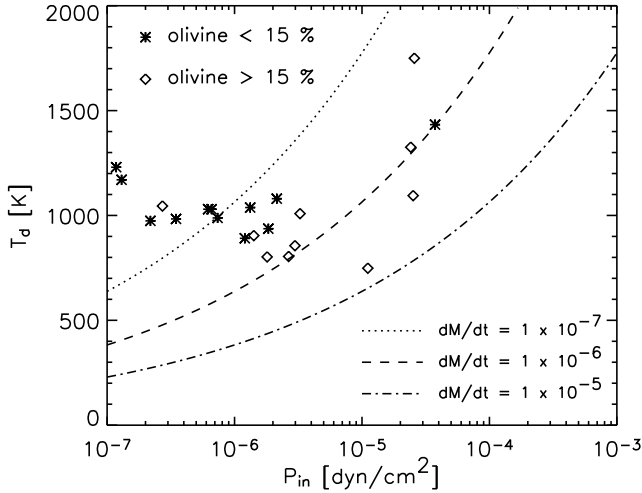


**Fig. 8.** Olivine content as a function of temperature and pressure at the inner edge of the dust shell. The lines represent regimes of constant mass-loss rate, as derived by Gail & Sedlmayr (1986).

1. the mass fraction of olivines increases
2. the melilite content decreases
3. the MgFeO content may decrease, but the Kendall test yields a low significance
4. the carbon and alumina content don't show a clear trend

Since the freeze-out scenario actually predicts different compositions for different temperature/pressure combinations in the wind, which of course depend on the mass-loss rate, we show the olivine content as a function of temperature and pressure at the inner edge of the dust shell in Fig. 8. It is clear from this figure that indeed, larger fractions of olivine dust are formed at higher wind densities as is predicted by the condensation sequence of Tielens (1990), and as is seen in AGB stars with low mass-loss rates (Heras & Hony 2005; Lebzelter et al. 2006).

## 8. Conclusions

We have analyzed the ISO-SWS spectra of 27 red supergiant stars, out of which 21 show significant mass loss through a dusty wind. The determined properties of the winds around RSG share some important characteristics with those around AGB stars with relatively low mass-loss rates. 1) The dust has a high fraction of "simple" dust species like metal-oxides. 2) The winds have a relatively low abundance of silicates. 3) The fraction of silicates correlates well with the mass-loss rate and/or the density and pressure at the base of the wind, as predicted by the canonical condensation sequence of Tielens (1990).

However, in some respects, RSG are not just the heavier twins of AGB stars: 1) They show molecular bands only of di-atomic molecules (not  $\text{H}_2\text{O}$ ,  $\text{CO}_2$  or  $\text{SO}_2$ ). 2) The general slope of the SED from near-IR to mid-IR wavelengths requires a source of continuous opacity which, in the case of RSG, could be due to amorphous carbon. 3) PAHs are observed in 4 sources, suggesting a strong influence by the chromospheric radiation field.

Besides the correlation observed by Josselin & Plez (2007) between photospheric turbulence strength and mass-loss rate, we find that also the stellar luminosity strengthens the wind.

Although the correlations and detections presented in this paper are significant (in a rough statistical sense) we are aware of possible 1) degeneracies between the fitting parameters, 2) biases due to our particular fitting strategy and model assumptions, and 3) biases due to our limited set of dust constituents.

Major progress will be possible in the near future with the 2nd generation VLTI instrumentation, in particular MATISSE (Lopez et al. 2006) will allow the quasi-instantaneous imaging of many RSG from the near to mid-IR. This will allow us to determine the actual spatial distribution of the different dust components.

**Acknowledgements.** The authors would like to thank the anonymous referee for many valuable comments, and C. Kemper for a careful reading of the manuscript. KE gratefully acknowledges support from the Swedish Research Council.

## References

- Arenou, F., Grenon, M., & Gomez, A. 1992, *A&A*, 258, 104  
 Beck, H. K. B., Gail, H.-P., Henkel, R., & Sedlmayr, E. 1992, *A&A*, 265, 626  
 Begemann, B., Dorschner, J., Henning, T., et al. 1997, *ApJ*, 476, 199  
 Bohren, C. F. & Huffman, D. R. 1983, *Absorption and scattering of light by small particles* (New York: Wiley, 1983)  
 Bouwman, J. 2001, PhD thesis, University of Amsterdam  
 Bouwman, J., de Koter, A., van den Ancker, M. E., & Waters, L. B. F. M. 2000, *A&A*, 360, 213  
 Cami, J. 2002, PhD thesis, AA(University of Amsterdam)  
 Cardelli, J. A., Clayton, G. C., & Mathis, J. S. 1989, *ApJ*, 345, 245  
 Chiar, J. E. & Tielens, A. G. G. M. 2006, *ApJ*, 637, 774  
 Cousins, A. W. J. & Lagerweij, H. C. 1971, *Monthly Notes of the Astronomical Society of South Africa*, 30, 12  
 de Graauw, T., Haser, L. N., Beintema, D. A., et al. 1996, *A&A*, 315, L49  
 Dijkstra, C., Speck, A. K., Reid, R. B., & Abraham, P. 2005, *ApJ*, 633, L133  
 Dorschner, J., Begemann, B., Henning, T., Jaeger, C., & Mutschke, H. 1995, *A&A*, 300, 503  
 Feautrier, P. 1964, *C.R.Acad.Sc.Paris*, 258, 3189  
 Gail, H.-P. & Sedlmayr, E. 1986, *A&A*, 166, 225  
 Gail, H.-P. & Sedlmayr, E. 1999, *A&A*, 347, 594  
 Gehrz, R. 1989, in *IAU Symposium, Vol. 135, Interstellar Dust*, ed. L. J. Allamandola & A. G. G. M. Tielens, 445–+  
 Gielen, C., van Winckel, H., Waters, L. B. F. M., Min, M., & Dominik, C. 2007, *A&A*, 475, 629  
 Gustafsson, B., Edvardsson, B., Eriksson, K., et al. 2008, *A&A*, 486, 951  
 Harper, G. M., Brown, A., & Lim, J. 2001, *ApJ*, 551, 1073  
 Harwit, M., Malfait, K., Decin, L., et al. 2001, *ApJ*, 557, 844  
 Henning, T., Begemann, B., Mutschke, H., & Dorschner, J. 1995, *A&AS*, 112, 143  
 Henning, T. & Stognienko, R. 1996, *A&A*, 311, 291  
 Heras, A. M. & Hony, S. 2005, *A&A*, 439, 171  
 Herbst, W. & Assousa, G. E. 1977, *ApJ*, 217, 473  
 Hoefner, S., Jorgensen, U. G., Loidl, R., & Aringer, B. 1998, *A&A*, 340, 497  
 Höfner, S. 2008, *A&A*, 491, L1  
 Höfner, S. & Andersen, A. C. 2007, *A&A*, 465, L39  
 Hony, S., Van Kerckhoven, C., Peeters, E., et al. 2001, *A&A*, 370, 1030  
 Humphreys, R. M. 1978, *ApJS*, 38, 309  
 Humphreys, R. M. & Ney, E. P. 1974, *ApJ*, 194, 623  
 Jaeger, C., Mutschke, H., Begemann, B., Dorschner, J., & Henning, T. 1994, *A&A*, 292, 641  
 Jennings, D. E. & Sada, P. V. 1998, *Science*, 279, 844  
 Johnson, H. L., Iriarte, B., Mitchell, R. I., & Wisniewski, W. Z. 1966a, *Communications of the Lunar and Planetary Laboratory*, 4, 99  
 Johnson, H. L., Mendoza V., & Eugenio, E. 1966b, *Annales d'Astrophysique*, 29, 525  
 Josselin, E. & Plez, B. 2007, *A&A*, 469, 671  
 Kemper, F., de Koter, A., Waters, L. B. F. M., Bouwman, J., & Tielens, A. G. G. M. 2002, *A&A*, 384, 585  
 Kessler, M. F., Stein, J. A., Anderegg, M. E., et al. 1996, *A&A*, 315, L27  
 Kharchenko, N. V. 2001, *Kinematika i Fizika Nebesnykh Tel.*, 17, 409  
 Kholopov, P. N., Samus, N. N., Frolov, M. S., et al. 1998, in *Combined General Catalogue of Variable Stars, 4.1 Ed (II/214A)*, (1998), 0–+  
 Koike, C., Kaito, C., Yamamoto, T., et al. 1995, *Icarus*, 114, 203  
 Kraemer, K. E., Sloan, G. C., Price, S. D., & Walker, H. J. 2002, *ApJS*, 140, 389  
 Lebzelter, T., Posch, T., Hinkle, K., Wood, P. R., & Bouwman, J. 2006, *ApJ*, 653, L145  
 Lee, T. A. 1970, *ApJ*, 162, 217

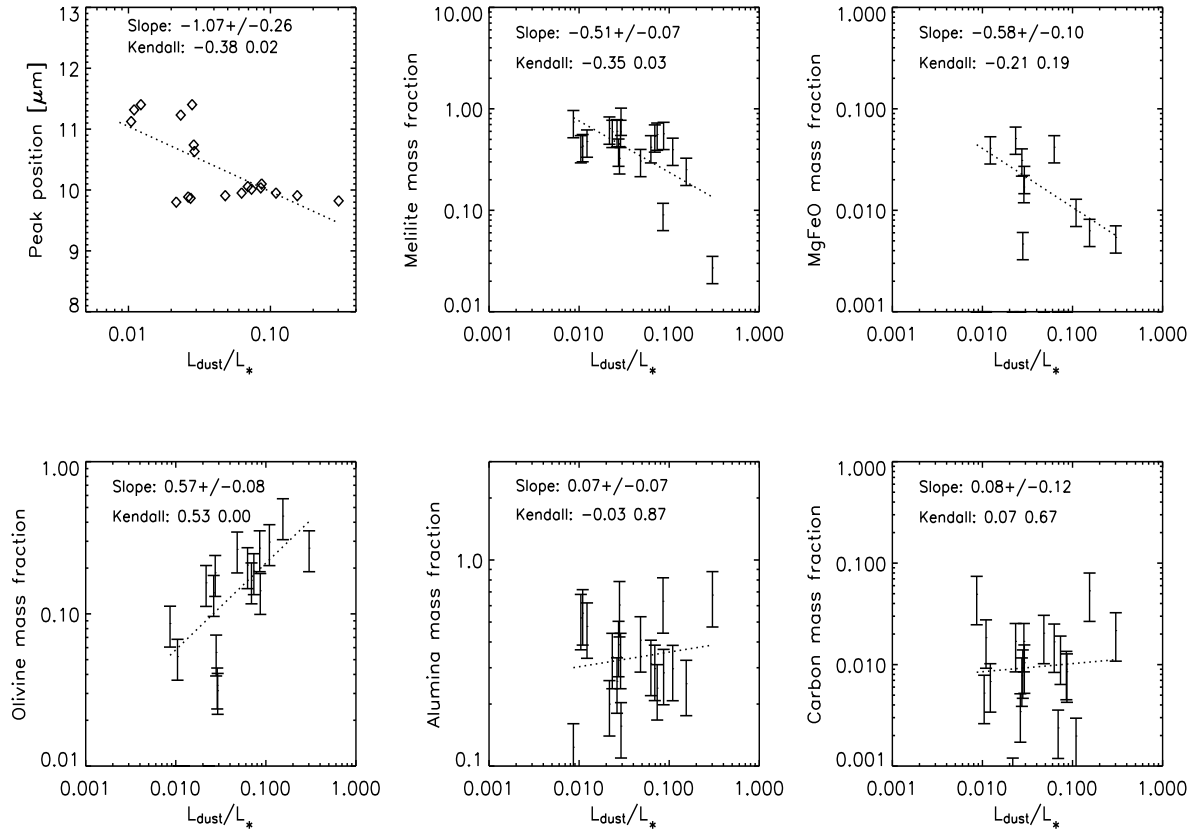


**Fig. 7.** Correlations between the different dust species and the mass-loss rate as traced by the dust luminosity (same analysis as in Fig. 6).

- Lejeune, T. & Schaerer, D. 2001, *A&A*, 366, 538  
 Levesque, E. M., Massey, P., Olsen, K. A. G., et al. 2005, *ApJ*, 628, 973  
 Lopez, B., Wolf, S., Lagarde, S., et al. 2006, in Presented at the Society of Photo-Optical Instrumentation Engineers (SPIE) Conference, Vol. 6268, *Advances in Stellar Interferometry*. Edited by Monnier, John D.; Schöller, Markus; Danchi, William C.. Proceedings of the SPIE, Volume 6268, pp. 62680Z (2006).  
 Massey, P. 2003, *ARA&A*, 41, 15  
 Massey, P., Plez, B., Levesque, E. M., et al. 2005, *ApJ*, 634, 1286  
 Mathis, J. S., Ruml, W., & Nordsieck, K. H. 1977, *ApJ*, 217, 425  
 Matsuura, M., Zijlstra, A. A., van Loon, J. T., et al. 2005, *A&A*, 434, 691  
 Mendoza, E. E. 1967, *Boletín de los Observatorios Tonantzintla y Tacubaya*, 4, 149  
 Mihalas, D. 1978, *Stellar atmospheres /2nd edition/* (San Francisco, W. H. Freeman and Co., 1978. 650 p.)  
 Min, M., Hovenier, J. W., & de Koter, A. 2005, *A&A*, 432, 909  
 Mutschke, H., Begemann, B., Dorschner, J., et al. 1998, *A&A*, 333, 188  
 Neugebauer, G., Habing, H. J., van Duinen, R., et al. 1984, *ApJ*, 278, L1  
 Nicolet, B. 1978, *A&AS*, 34, 1  
 Ohnaka, K. 2004, *A&A*, 424, 1011  
 Peeters, E. 2002, PhD thesis, Proefschrift, Rijksuniversiteit Groningen, 2002, 237 p.  
 Perrin, G., Ridgway, S. T., Mennesson, B., et al. 2004, *A&A*, 426, 279  
 Perrin, G., Ridgway, S. T., Verhoelst, T., et al. 2005, *A&A*, 436, 317  
 Perrin, G., Verhoelst, T., Ridgway, S. T., et al. 2007, *ArXiv e-prints*, 709  
 Perryman, M. A. C., Lindegren, L., Kovalevsky, J., et al. 1997, *A&A*, 323, L49  
 Preibisch, T., Ossenkopf, V., Yorke, H. W., & Henning, T. 1993, *A&A*, 279, 577  
 Ryde, N., Richter, M. J., Harper, G. M., Eriksson, K., & Lambert, D. L. 2006, *ApJ*, 645, 652  
 Skrutskie, M. F., Cutri, R. M., Stiening, R., et al. 2006, *AJ*, 131, 1163  
 Sloan, G. C., Kraemer, K. E., Price, S. D., & Shipman, R. F. 2003, *ApJS*, 147, 379  
 Speck, A. K., Barlow, M. J., Sylvester, R. J., & Hofmeister, A. M. 2000, *A&AS*, 146, 437  
 Sylvester, R. J., Barlow, M. J., & Skinner, C. J. 1994, *MNRAS*, 266, 640  
 Sylvester, R. J., Skinner, C. J., & Barlow, M. J. 1998, *MNRAS*, 301, 1083  
 Tielens, A. G. G. M. 1990, in *From Miras to Planetary Nebulae: Which Path for Stellar Evolution?*, ed. M. O. Mennessier & A. Omont, 186–200  
 Tsuji, T. 2000, *ApJ*, 538, 801  
 van Boekel, R., Min, M., Waters, L. B. F. M., et al. 2005, *A&A*, 437, 189  
 Verhoelst, T., Decin, L., van Malderen, R., et al. 2006, *A&A*, 447, 311  
 Wawrukiewicz, A. S. & Lee, T. A. 1974, *PASP*, 86, 51  
 Woitke, P. 2006, *A&A*, 460, L9  
 Woitke, P. & Niccolini, G. 2005, *A&A*, 433, 1101